

# Elucidation of Metal Local Environments in Single-Atom Catalysts Based on Carbon Nitrides

Simon Büchele, Alexander Yakimov, Sean M. Collins, Andrea Ruiz-Ferrando, Zupeng Chen, Elena Willinger, Demie M. Kepaptsoglou, Quentin M. Ramasse, Christoph R. Müller, Olga V. Safonova, Núria López, Christophe Copéret, Javier Pérez-Ramírez,\* and Sharon Mitchell\*

The ability to tailor the properties of metal centers in single-atom heterogeneous catalysts depends on the availability of advanced approaches for characterization of their structure. Except for specific host materials with well-defined metal adsorption sites, determining the local atomic environment remains a crucial challenge, often relying heavily on simulations. This article reports an advanced analysis of platinum atoms stabilized on poly(triazine imide), a nanocrystalline form of carbon nitride. The approach discriminates the distribution of surface coordination sites in the host, the evolution of metal coordination at different stages during the synthesis of the material, and the potential locations of metal atoms within the lattice. Consistent with density functional theory predictions, simultaneous high-resolution imaging in high-angle annular dark field and bright field modes experimentally confirms the preferred localization of platinum in-plane in the corners of the triangular cavities. X-ray absorption spectroscopy (XAS), X-ray photoelectron spectroscopy (XPS), and dynamic nuclear polarization enhanced  $^{15}\text{N}$  nuclear magnetic resonance (DNP-NMR) spectroscopies coupled with density functional theory (DFT) simulations reveal that the predominant metal species comprise Pt(II) bound to three nitrogen atoms and one chlorine atom inside the coordination sites. The findings, which narrow the gap between experimental and theoretical elucidation, contribute to the improved structural understanding and provide a benchmark for exploring the speciation of single-atom catalysts based on carbon nitrides.


## 1. Introduction

Advances in the precision design of catalysts rely on the refinement of structure-function relations. In heterogeneous catalysis, the development of single-atom catalysts (SACs), in which a minority element, commonly a transition metal, is stabilized as isolated atoms on a suitable host material and attracted significant interest for potentially reducing the diversity of active sites.<sup>[1]</sup> Site uniformity is appealing for enabling specific reactivity and simplifying structure elucidation, thus allowing method benchmarking, which has prompted intense efforts toward the precise design of tailored structures.<sup>[2]</sup> Nonetheless, since most commonly applied host materials contain a variety of metal coordination sites, different single metal atoms anchored on the same support may have distinct geometric and electronic structures, resulting in distinct reactivity.<sup>[3]</sup> This nonuniformity of the active metal species poses an additional challenge for determining the atomic architecture based on established methods.<sup>[4]</sup>

S. Büchele, A. Yakimov, C. Copéret, J. Pérez-Ramírez, S. Mitchell  
Department of Chemistry and Applied Biosciences  
ETH Zurich

Vladimir-Prelog-Weg 1, Zurich 8093, Switzerland  
E-mail: jpr@chem.ethz.ch; sharon.mitchell@chem.ethz.ch

S. M. Collins  
Bragg Centre for Materials Research  
School of Chemical and Process Engineering and School of Chemistry  
University of Leeds  
Leeds LS2 9JT, UK

 The ORCID identification number(s) for the author(s) of this article can be found under <https://doi.org/10.1002/sml.202202080>.

© 2022 The Authors. Small published by Wiley-VCH GmbH. This is an open access article under the terms of the Creative Commons Attribution-NonCommercial License, which permits use, distribution and reproduction in any medium, provided the original work is properly cited and is not used for commercial purposes.

DOI: 10.1002/sml.202202080

A. Ruiz-Ferrando, N. López  
Institute of Chemical Research of Catalonia and Barcelona  
Institute of Science and Technology  
Av. Països Catalans 16, Tarragona 43007, Spain

Z. Chen  
College of Chemical Engineering  
Nanjing Forestry University  
Nanjing 210037, P. R. China

E. Willinger, C. R. Müller  
Department of Mechanical and Process Engineering  
ETH Zurich  
Leonhardstrasse 21, Zurich 8092, Switzerland

D. M. Kepaptsoglou, Q. M. Ramasse  
SuperSTEM Laboratory  
SciTech Daresbury Campus  
Daresbury WA4 4AD, UK

O. V. Safonova  
Paul Scherrer Institute  
Forschungsstrasse 111, Villigen 5232, Switzerland

The experimental characterization of SACs relies on multi-technique approaches, typically involving the combination of imaging and spectroscopic tools.<sup>[5]</sup> Atomic-resolution imaging via aberration-corrected scanning transmission electron microscopy (AC-STEM) can confirm the presence of atomically-dispersed metals, provided there is sufficient atomic-number dependent contrast from the host.<sup>[6]</sup> For systems with more ideal structures for imaging, such as single atoms on individual graphene layers,<sup>[7]</sup> precious metals in well-defined positions on crystalline metal oxides (e.g., Pt/TiO<sub>2</sub> or Pt/CeO<sub>2</sub>),<sup>[8]</sup> or single-atom alloys (e.g., Pt/Cu),<sup>[9]</sup> metal coordination environments including the atomic structure of the carrier can also be directly visualized. Nonetheless, beam-induced structural damage to the hosts and mobility of metal atoms due to the interaction with high-energy electrons makes structure verification through imaging very challenging for many hosts.<sup>[10]</sup> X-ray absorption spectroscopy (XAS) can contribute powerful complementary insights into the coordination sphere, but extracting the signatures of coexisting structural environments remains challenging.<sup>[11]</sup> Consequently, constructing structural models of SACs often relies on ab-initio simulations guided by the most likely scenarios determined from experimental data.<sup>[12]</sup>

A prominent class of SAC hosts for which most structural understanding derives from theoretical insights is carbon nitrides.<sup>[13,14]</sup> This (semi-)crystalline family of materials offers unique potential for stabilizing single atoms because their lattice structures contain highly coordinative nitrogen-containing macrocycles that potentially offer abundant, well-defined, and tailorable surface metal coordination sites.<sup>[15]</sup> The most widely applied form is understood to consist of graphitic heptazine-based layers, often exfoliated to generate high-surface-area analogs. Other common forms include partially-polymerized linear melem oligomers as well as more highly ordered poly(triazine imides) or poly(heptazine imides), which exhibit promising properties, especially in photocatalysis.<sup>[16]</sup> The ordered atomic arrangements simplify the modeling of SACs based on carbon nitrides, but questions remain about the accuracy and prevalence of predicted structures.<sup>[17]</sup> In particular, experimental verification of the predictions proves to be complex due to the high beam sensitivity of these materials, the possible coexistence of structures between which XAS cannot distinguish, and the limited chemisorption of common probe molecules. Furthermore, the types and contributions of defects in nanocrystalline high-surface forms and the presence of various dynamically-interconnected coordination sites within the lattice are often not addressed.<sup>[17]</sup>

Toward closing the gap between predicted and experimentally-evidenced geometric and electronic structures of single-atom catalysts based on carbon nitrides, we focused on the fully condensed poly(triazine imide) form (ideal formula (C<sub>3</sub>N<sub>3</sub>)<sub>2</sub>(NH<sub>x</sub>Li<sub>1-x</sub>)<sub>3</sub> · LiCl, where  $x = 2/3$ ). The improved uniformity of surface coordination sites in this host, as confirmed through surface-sensitive characterization, facilitates the determination of atomic environments of anchored metal species. Simultaneous AC-STEM imaging under optimized sample preparation and acquisition parameters in bright- (BF) and high-angle annular dark- (HAADF) field modes permits the localization of platinum atoms on the host lattice. As the coordination sphere of metal centers depends on the synthesis

conditions and the associated removal of ligands and bonding to the host, we monitored the evolution of the geometric and electronic properties at different stages of the stabilization and activation of the metal precursor. Specifically, changes in the oxidation state and coordination sphere of metal centers and their interaction with the host are followed by X-ray photoelectron (XPS), XAS, and dynamic nuclear polarization surface-enhanced <sup>15</sup>N NMR (DNP-SENS) spectroscopies, respectively. The experimentally determined structures agree well with those derived from density functional theory (DFT) simulations, showing that the predominant metal species comprise Pt(II) bound to three nitrogen atoms and one chlorine atom inside the coordination pockets of the poly(triazine imide) structure. Our results highlight the importance of considering distributions of active-site structures and demonstrate the power of integrated, multi-probe techniques to identify the metal-support interactions in carbon nitrides, necessary to develop improved design principles for single-atom catalysts.

## 2. Results and Discussion

### 2.1. Analysis of Carrier Properties

The synthesis of carbon nitrides occurs via the condensation of nitrogen-rich precursors (e.g., urea, dicyandiamide, or melamine) into discrete oligomers, polymers, and more extended networks. However, incomplete polymerization often limits structural development. Ionothermal syntheses using eutectic mixtures of LiCl and KCl can overcome underlying kinetic limitations, resulting in highly crystalline structures. Here, we prepared two poly(triazine imide) hosts, a standard (PTI) form prepared via the polymerization of melamine in a LiCl–KCl salt melt and a high-crystallinity model analog (HC-PTI) prepared using only LiCl, which was primarily used for the imaging analysis.<sup>[18]</sup>

Characterization by multiple techniques provided insights into the types and uniformity of surface coordination sites in the resulting metal-free hosts (**Figure 1**; Figures S1 and S2, Supporting Information). Analysis of the metal-free hosts by aberration-corrected scanning transmission electron microscopy (AC-STEM) confirmed the expected atomic structure and generally high crystallinity of HC-PTI (Figure 1a,b). The hexagonal structural motifs viewed along the [001] direction (Figure 1a) arise from the alternate stacking of triangular cavities, with the central white spot corresponding to rows of chlorine ions, matching the intensity patterns observed in the simulated micrographs. Nonetheless, variation in the positions of the bright spots attributed to atomic columns of chlorine, which are not always perfectly centered, evidence some flexibility or disorder of the carrier structure, possibly relating to stacking defects (Figure S3, Supporting Information). The planes viewed along the [100] direction display a lattice spacing of 0.73 nm, agreeing with reported values.<sup>[19]</sup>

The ideal structure of poly(triazine imide) contains only one type of chemically equivalent carbon and two types of nitrogen nuclei, namely C-NH-C ( $N_a$ ) and pyridinic nitrogen ( $N_b$ ) (shown schematically in Figure 1c inset). Consistently, fitting the N 1s XPS spectra identified two principal peaks

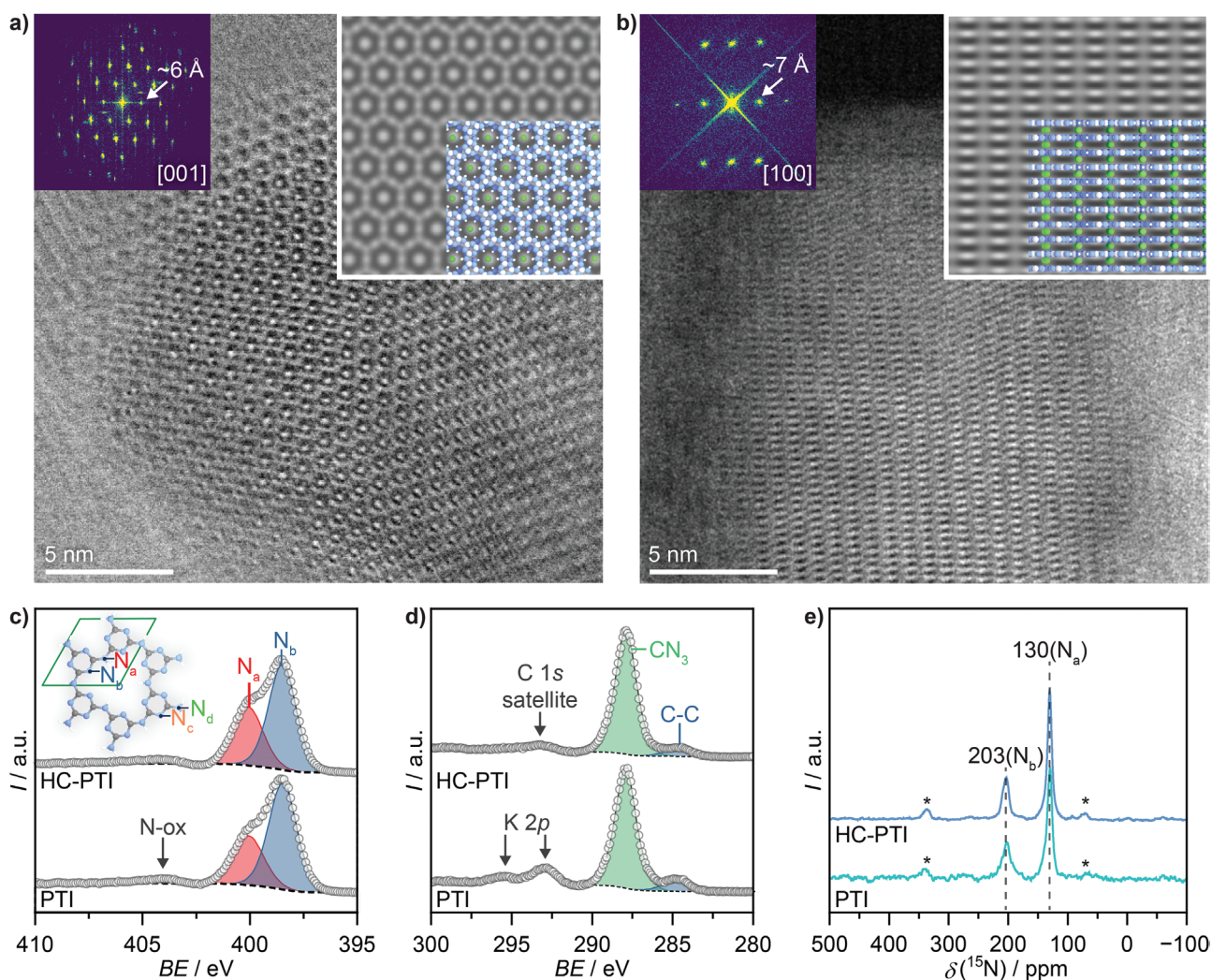


**Figure 1.** a) Annular bright-field (top left) and b) annular dark-field (top right) STEM images (300 kV) along the [001] and [100] directions of the metal-free HC-PTI carrier, respectively. Insets show the corresponding Fourier transforms and simulated images with schemes of the structure overlaid. c) N 1s, d) C 1s XPS, and e) DNP-enhanced  $^1\text{H}$ - $^{15}\text{N}$  CP/MAS NMR spectra of metal-free PTI and HC-PTI. The inset in c) shows a structural model of PTI indicating the unit cell and distinct nitrogen sites ( $N_{a-d}$ ). Stars in (e) denote spinning sidebands. Atom coloring: C, grey; H, white; and N, blue.

( $N_a$  at  $398.4 \pm 0.2$  eV and  $N_b$  at  $400.0 \pm 0.2$  eV) together with a small contribution of highly oxidized nitrogen defects appearing at high binding energies (Figure 1c). Similarly, analysis of the C 1s XPS spectra revealed a single prominent peak at 2879 eV (Figure 1d, position fixed for reference purposes). Although consistent with previous reports (Table S1, Supporting Information),<sup>[14]</sup> comparison of the bulk composition to an idealized stoichiometry with one LiCl ion pair per coordination pocket shows that some of the templating salt was removed during the washing steps, resulting in reduced Li and Cl contents. DFT simulations show a thermodynamic preference for a distribution of  $\text{Li}^+$  ions throughout the structure over the accumulation of multiple ions in one cavity. This distribution leaves room for transition metals to coordinate in the same cavities (see below).

The uniformity of surface nitrogen sites was further probed by performing dynamic nuclear polarization (DNP)-enhanced  $^1\text{H}$ - $^{15}\text{N}$  cross-polarization magic angle spinning (CP/MAS) NMR spectroscopy. The TEKPol radical, introduced in the

sample as a 1,1,2,2-tetrachloroethane (TCE) solution, was used to drive polarization transfer through the protons of the solvent to surface  $^{15}\text{N}$  nuclei.<sup>[20]</sup> By enhancing signals from TCE and surface  $^{15}\text{N}$  nuclei 24-fold and 17-fold, respectively, the use of DNP-SENS (surface-enhanced NMR spectroscopy) overcomes known NMR sensitivity issues for  $^{15}\text{N}$  nuclei (low gamma, 0.4% natural abundance),<sup>[21]</sup> reducing measurement times by 300-fold, and thereby enabling the study of materials without isotopic enrichment. The spectra observed for PTI and HC-PTI materials further evidenced the predominance of two nitrogen species at  $\approx 130$  and 203 ppm (Figure 1e). Based on previous reports, these features relate to  $N_a$  and  $N_b$  species, respectively.<sup>[22]</sup> DFT simulations using cluster models cut from periodic models (see Experimental Section for details) corroborate this assignment with calculated chemical shifts of 128 ppm ( $N_a$ ) and 201 ppm ( $N_b$ ). Nitrogen species associated with surface defects at the cluster edges ( $N_c$  and  $N_d$ ) are expected to appear at 187 and 67 ppm, respectively. The absence of the latter



signals in the spectra indicates that the concentration of defects is below detection limits, pointing to a high degree of order in both the PTI and HC-PTI materials, presenting a suitable basis for characterizing coordination environments of stabilized metal species.

## 2.2. Imaging Metal Atoms Anchored on HC-PTI

Aberration-corrected scanning transmission electron microscopy (AC-STEM) in annular dark field mode is among the most widely used techniques to confirm the atomic dispersion of metals in single-atom catalysts. Although most transition metals are readily observable on light crystalline carriers such as carbon nitride, we are not aware of any studies that have localized the position of metal centers onto lattice positions (Figure 2a; Figure S4 (Supporting Information) show typical images). The difficulty arises due to the high beam

sensitivity of these materials, which rapidly results in metal atom displacements (i.e., knock-on damage) and complete loss of crystalline order due to ionization and bond-breaking (i.e., radiolysis) even under cryogenic conditions. Overcoming this challenge requires the development of approaches that sufficiently minimize the electron beam damage to extract intrinsic structural information. Here, dispersion of the specimen on grids coated with graphene monolayers improved the stability during image acquisition. Supporting or sandwiching beam-sensitive specimens in graphene has been previously shown to improve their stability of otherwise ionization-afflicted systems, which was proposed to originate from the availability of electrons in the support.<sup>[23]</sup> Selection of the electron beam current, exposure time, and pixel size focused on balancing sufficient signal-to-noise for single metal atom visibility while minimizing beam-induced changes. This balance incorporates both intrinsic factors, such as the rate of damage in the sample under electron beam exposure, and extrinsic factors,

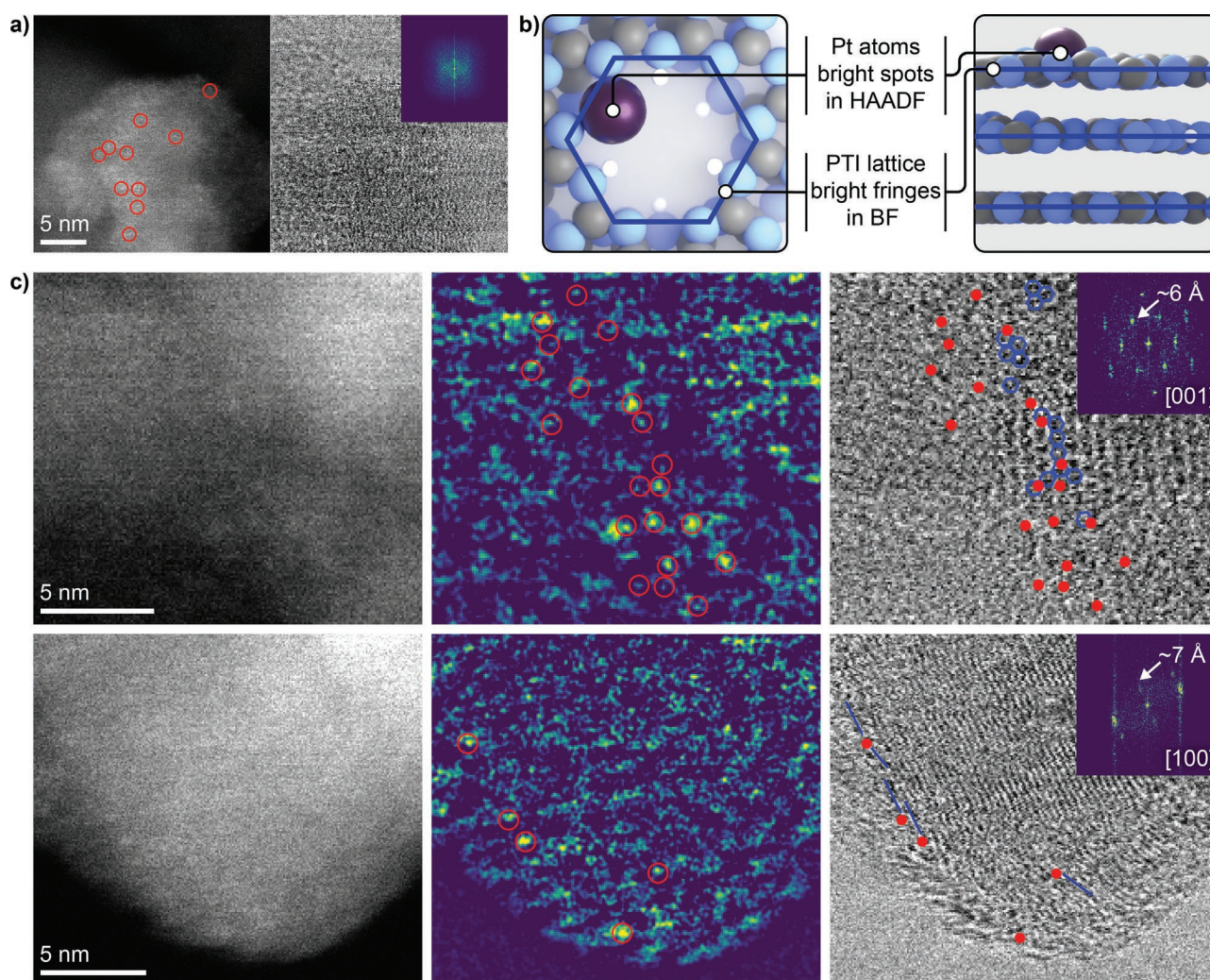


**Figure 2.** a) HAADF- and BF- (Fourier transform inset) ASTEM images (60 kV) of a disordered or amorphous area of Pt/HC-PTI. b) Scheme and c) application of simultaneous HAADF-BF STEM imaging for mapping Pt atoms onto the lattice of poly(triazine imide) along the [001] and [100] directions. From left to right: HAADF-STEM, filtered HAADF-STEM (red circles indicate identified Pt atoms), and BF-STEM images with Fourier transform inset (blue hexagons mark the crystalline motif, red dots show the respective positions of Pt atoms) of Pt/HC-PTI in different locations. Atom identification is not attempted in the thickest (brightest) regions in HAADF-STEM. Atom coloring: C, grey; H, white; N, blue; and Pt, purple.



such as the signal-to-noise determined by the detector systems. Our approach was to first identify imaging conditions (exposure time at each pixel for a given beam current) with an inadequate signal-to-noise ratio and then to increase the exposure to recover images with just a satisfactory signal-to-noise ratio in 1–2 acquisitions. The simultaneous acquisition of HAADF- and BF-STEM images prioritizes the sensitivity to atomic number contrast at high scattering angles to reliably distinguish platinum atoms anchored on HC-PTI with phase-contrast enabling their correlation to the carrier lattice (Figure 2b,c).

Due to the constraints on the number of frames acquired and variations in sample height, individual crystallites are generally not perfectly focused within the available dose budget prior to the loss of observable crystalline order. The BF-STEM signal enables imaging of the carrier lattice away from zero defocus, while the simultaneous HAADF-STEM signal records the relatively brighter intensity of the Pt atoms within a depth of field of a few nanometers (even when the lattice is not resolved in HAADF-STEM) enabling correlation with the carrier structure. Depending on specific imaging parameters, BF-STEM can suffer from contrast ambiguity, where bright or dark features may correspond to the atomic positions. Comparison with the simulated hexagonal motif (Figure 1a) and the detected HAADF-STEM intensity (with a bright signal at atom columns) at small defocus (Figure 2c; Figure S5, Supporting Information) indicates that the atom columns in the poly(triazine imide) lattice corresponded to bright intensity in BF-STEM under the similar imaging and focusing conditions used across the measurements. In some cases, Fourier filtering was applied to regions of BF-STEM images containing crystallographic information to improve the visualization of the lattice (Figure S5, Supporting Information). Separate image processing was also applied to the HAADF-STEM micrographs to corroborate atom identification. In both cases, we consistently show unfiltered data for comparison.

Analysis of many different regions of a platinum single-atom catalyst based on HC-PTI (Pt/HC-PTI, containing 0.5 wt.% Pt) provides insight into the uniformity of metal locations (Figure 2c, Figures S5–S12, Supporting Information). The absence of larger clusters or nanoparticles in any of the regions studied agrees with the comparatively low metal content in the Pt/HC-PTI sample. Ensuring a representative assessment is important as any individual example will exhibit some ambiguity in atom location due to both the variety of possible anchoring sites of single atoms on the 3D carrier particles and beam-induced changes in the sample beginning at the instant the electron beam interacts with the sample. Multiple instances of similar characteristic atom locations, however, depict a consistent arrangement, which improves confidence in inferring the characteristic features of Pt binding from many candidate atom locations. Based on the preparative approach and the observations from the surface-sensitive spectroscopic analysis, we expect the majority of atoms to reside at the crystal surfaces rather than in the bulk of the carrier. The lack of visible atoms in the interlayer regions when viewed parallel to the layers of the poly(triazine imide) structure suggests that the metal strongly prefers in-plane positions. Although more difficult to precisely define, when observed perpendicular to the layer, metal atoms appear to sit preferentially at sites close to the corners of the

hexagonal motifs. Metal atoms are also commonly observed in less-ordered regions between planes, highlighting the potential diversity of lattice sites and associated speciation of anchored metals. Obtaining insights about the local structures in these positions is not straightforward. Due to their coexistence with crystalline domains, the amorphous regions observed in the sample appear to reflect the structure of the fresh catalyst rather than resulting from beam-induced damage.

Despite their low atomic number, the high number of carbon or nitrogen atoms in atomic columns imaged in projection complicates the identification of metal atoms, which comprises a challenge in analyzing crystalline supports. Nonetheless, similar conclusions regarding the location of platinum centers could be drawn from a separate analysis of palladium atoms anchored on HC-PTI at 300 kV (Figure S13, Supporting Information). However, it was not possible to locate palladium atoms in the images, even though they could be clearly identified following loss of the carrier structure and the presence of palladium was evidenced by energy-dispersive X-ray spectroscopy (Figure S14, Supporting Information). Taken together, the STEM data confirm the representativeness of the structures simulated by DFT, supporting the preferential location of single metal atoms in plane very close to the edges of the triangular cavities. Correlation of the anchored metal species to the lattice of the carrier offers unprecedented insight into the uniformity of their distribution, which can be connected to the carrier properties and synthesis method. Further work to understand and optimize these properties will require the adoption of automated approaches for imaging and image analysis<sup>[24]</sup> to extract statistically-relevant descriptors for designing improved catalysts.

### 2.3. Spectroscopic Insights into the Metal Coordination

The stabilization of platinum atoms on the poly(triazine imide) carriers followed a recently reported protocol involving introducing the metal precursor by wet deposition followed by a two-step thermal activation with intermediate washing.<sup>[25]</sup> During this procedure, a low-temperature thermal annealing step induces the partial decomposition of the hexachloroplatinic acid precursor and the initial bonding of the metal to the carrier. Subsequent washing removes residual loosely bound species, while a second high-temperature treatment in an inert atmosphere controls the removal of the remaining ligands (Figure 3a; Table S2, Supporting Information describes the specific preparation conditions for all samples). Isolation of samples after each stage of the treatment permitted elucidation of the evolution in the coordinating environment during the metal introduction (Figure 3a), targeting a platinum content of 5 wt.% to ensure a good signal for spectroscopic analyses.

Quantification of the bulk composition reveals a platinum content of 4 wt.% after the first activation (Pt<sub>A1</sub>/PTI) that reduces to 2 wt.% in the resulting single-atom catalyst (Pt/PTI-773), revealing that a significant fraction of the metal remains loosely bound after the first annealing (Figure S15, Supporting Information). The amount of lithium template remains relatively constant (3.5 wt.%) throughout the process, while the potassium content decreases slightly after washing. Analysis

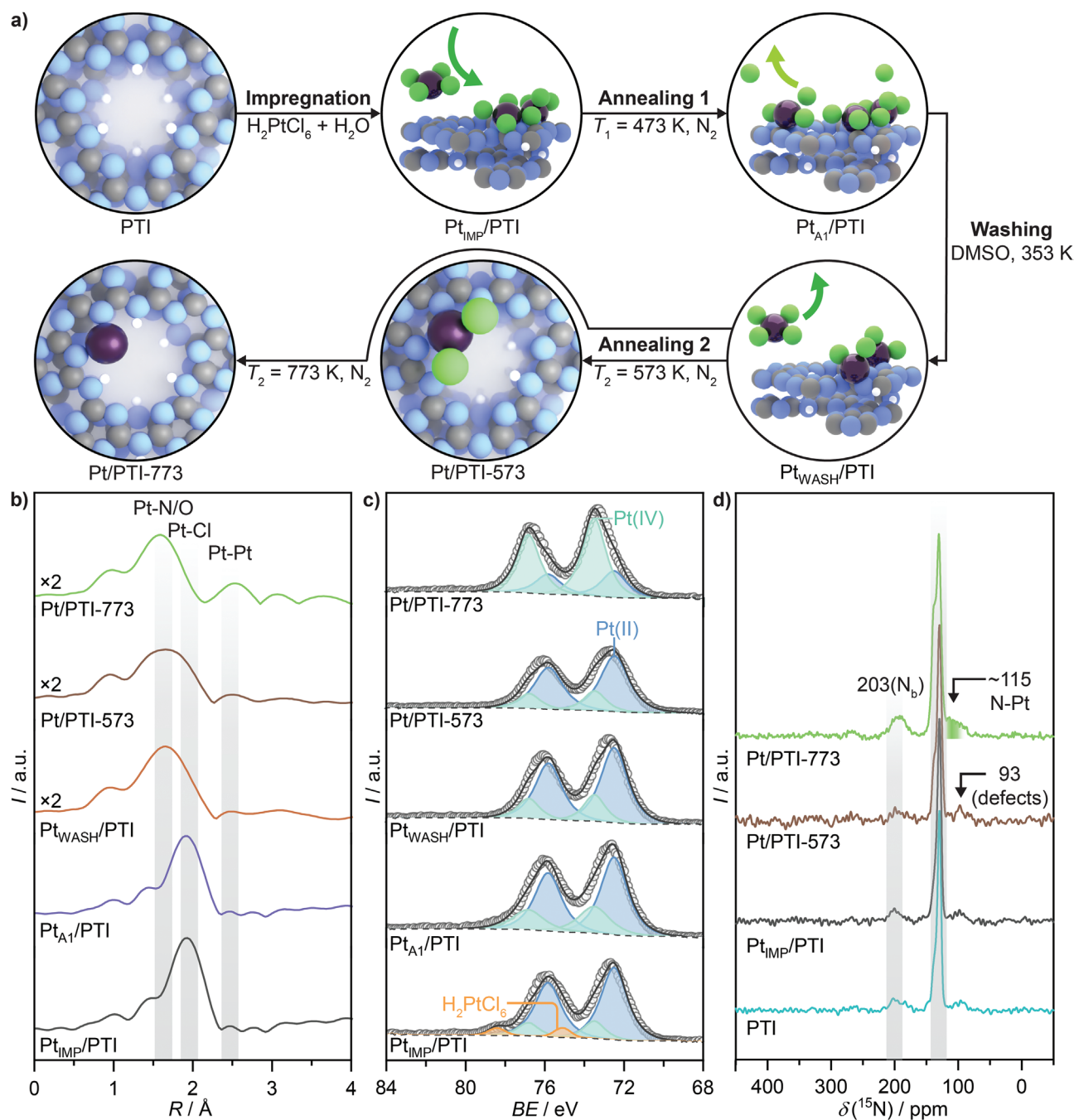


**Figure 3.** a) Synthetic steps during the stabilization of platinum atoms on poly(triazine imide) indicating the conditions and sample nomenclature. b) Pt 4f XPS spectra, c) Pt 4f EXAFS spectra, and d) DNP-enhanced  $^1\text{H}$ - $^{15}\text{N}$  CP/NMR spectra following structural changes in the carrier and in the coordination and electronic state of platinum during the metal deposition procedure. Reference spectra for EXAFS are shown in Figure S16 (Supporting Information). Atom coloring: C, grey; H, white; N, blue; Cl, green; and Pt, purple.

of the surface chlorine content by XPS shows that this initially increases upon addition of the chlorinated metal species but returns to values similar to the metal-free catalyst after annealing at 773 K, indicating that this temperature is sufficient to remove residual ligands from the metal center. The Pt 4f XPS spectra show that the majority of the metal precursor is reduced after impregnation ( $\text{Pt}_{\text{IMP}}/\text{PTI}$ ), evidencing the primary contribution of Pt(II) species ( $72.4 \pm 0.1$  eV) with a

minor component assigned to Pt(IV) ( $73.6 \pm 0.1$  eV) based on reference values (Figure 3b; Table S3, Supporting Information). A small contribution of the hexachloroplatinic acid precursor is observed at high binding energy ( $\approx 75.1$  eV),<sup>[26]</sup> but disappears after the first annealing step. Pt(II) is the predominant species in all materials except Pt/PTI-773, which is more oxidized, suggesting an increased interaction of metal centers with the carrier after thermal activation at 773 K.



Analysis by XAS (Pt  $L_3$ -edge) provides more insight into the coordination sphere and electronic properties of platinum species during the metal introduction (Figure 3c, fits reported in Table S4, Supporting Information, reference data in Figure S16, Supporting Information). The extended X-ray absorption fine structure (EXAFS) spectra reveal a dominant contribution, centered  $\approx 1.9$  Å in the Fourier transform, indicative of predominantly Pt-Cl coordination following wet deposition of the metal precursor and the first thermal activation (Pt<sub>IMP</sub>/PTI and Pt<sub>AI</sub>/PTI).

Consistently, the EXAFS fits evidence coordination numbers (CN) of  $5.4(\pm 0.4)$  and  $4.4(\pm 0.3)$ , respectively, in the Pt-Cl shell. The fact that the controlled coordination of Pt to the scaffold, resulting in a Pt-N interaction, is not detected after the first annealing likely arises because of the presence of an excess of chlorinated Pt precursor, removed by the subsequent washing step. The significant reduction in the Pt-Cl peak and increased contribution of the Pt-N coordination shell at  $\approx 1.6$  Å observed in Pt<sub>WASH</sub>/PTI support this hypothesis (CN =  $2.5 \pm 0.4$ ). The effect of the final annealing depends on the temperature. The sample annealed at 573 K (Pt/PTI-573) still contains both Pt-N and Pt-Cl coordination spheres. Comparatively, treatment of the washed sample at 773 K causes a further shortening of the dominant peak in the radial distribution function. The Pt-Cl contribution vanishes, and Pt-N becomes the main coordination shell of the metal, consistent with the coordination with the carrier (CN =  $3.5 \pm 0.8$ ). Although single atoms are the primary species in these samples, as confirmed in typical ADF-STEM images (Figure S4, Supporting Information) the presence of some subnanometer platinum clusters cannot be excluded and a small Pt-Pt contribution (CN =  $3.7 \pm 3.4$ ) is evidenced by the EXAFS fits. However, the large error in the coordination number suggests that the fraction of clusters is negligible. Analysis of the Pt  $L_3$  X-ray absorption near edge structure spectra evidences structural differences between the samples at different stages of preparation (Figure S17, Supporting Information). However, deconvoluting the effect of the oxidation state, nature of the ligand, and coordination number remains highly complex and cannot be addressed by a simple linear combination fitting.

Complementary to the study of the metal center, analysis of the coordinating species yields more information about the structure of the coordination site. For this purpose, DNP-enhanced  $^{15}\text{N}$  NMR spectroscopy, which is much more sensitive to the local surrounding of nuclei, has enabled observation of an additional broad signal centered at  $\approx 115$  ppm in the catalyst obtained by thermal activation at 773 K (Figure 3d, Pt/PTI-773). This feature, which was not present at earlier stages of the catalyst preparation, could relate to nitrogen sites in PTI coordinated with Pt. The absence of a similar peak in the spectra of the metal-free carrier subjected to equivalent treatments, but without adding the metal precursor, supports this assignment (Figure S18, Supporting Information). DFT simulations of the isotropic  $^{15}\text{N}$  chemical shifts using cluster models of poly(triazine imide) with Pt located within the coordination pockets indicate a change of 77 ppm due to the coordination of pyridinic nitrogen (203 ppm). Comparatively, chemical shifts of 101 and 114 ppm for the ion-free PTI and 106 and 111 ppm for the  $\text{Li}_2\text{Cl}_2$ -containing carrier are obtained for Pt atoms bound

to one Cl, two pyridinic nitrogens ( $N_b$ ), and one deprotonated aminic nitrogen ( $N_a$ ). The latter values are slightly closer to the experimentally observed shifts. However, given the appreciable linewidth obtained, both models are in good agreement with the experimental data.

#### 2.4. Simulations of Platinum on Poly(triazine imide)

Computational chemistry has become a powerful tool to investigate the nature of active sites in SACs, permitting the exploration of a vast range of possible metal-support interactions even though they may be difficult to verify experimentally. Nonetheless, bringing the conclusions of experimental observations and simulations together is crucial to build confidence in the predicted results. In the current Pt/PTI systems, the presence of LiCl distributed over the layers of the scaffold and the ability of Pt to exhibit different coordination environments widens the scenario of structures that need to be studied, calling for models that reproduce experimental conditions. For this reason, we conducted DFT simulations of the evolution of the speciation of platinum upon stabilization on poly(triazine imide) to compare the results with the experimental observations and examine the robustness of the predicted structures. Starting from the scaffold, the solvated precursor ( $\text{PtCl}_6^{2-}$ ),  $\text{Cl}_2$ , HCl, and LiCl, we determined binding Gibbs free energies of the different Pt-containing structures and their corresponding core-level shifts at 773 K (Figure 4; Table S5, Supporting Information).

To this end, a four-layer slab of poly(triazine imide) with 9N per cavity and an alternate stacking of the triangular cavities was used for the simulations, matching the hexagonal structural motifs identified by AC-STEM in projection. Consistent with the bulk chemical composition, the models considered a LiCl content of zero or one per cavity. The template ions are presumably distributed uniformly over the carrier since the aggregation of each pair of LiCl has a thermodynamic penalty of at least 0.2 eV (Table S6, Supporting Information), agreeing with the observation of regularly distributed atomic columns of Cl. Accordingly, we explored the adsorption of the Pt precursor when placed at the center of a salt-free poly(triazine imide) cavity or on an analog containing a single LiCl pair, with subsequent removal of chlorine and hydrogen chloride to the gas-phase reservoir. The adsorption of  $\text{PtCl}_6^{2-}$  over a cavity containing two LiCl pairs was also explored to examine the potential stabilizing effect of LiCl on the distinct Pt structures. The simulations show that  $\text{Li}^+$  ions preferentially reside at the corners of the triangular cavities in the carrier, interacting with Cl ligands placed at the center (Figure S19, Supporting Information).

The adsorption of  $\text{PtCl}_6^{2-}$  over the salt-free poly(triazine imide) cavity leads to the formation of  $\text{PtCl}_4^*$  ( $-0.62$  eV). The subsequent loss of chlorine ligands induces the formation of  $\text{PtCl}_2^*$  ( $-0.66$  eV), coinciding with the immediate reduction of the precursor observed by XPS. Even mono-Cl and Cl-free species, namely  $\text{PtCl}^*(-\text{H})$ ,  $-0.15$  eV and  $\text{Pt}_{(\text{s})}^*(-2\text{H})$  ( $1.57$  eV) can form by enforcing the release of chlorine upon annealing. Changes in the coordination environment of platinum atoms due to the loss of chlorine ligands strengthen their interaction with the scaffold, potentially leading to higher core-level shifts

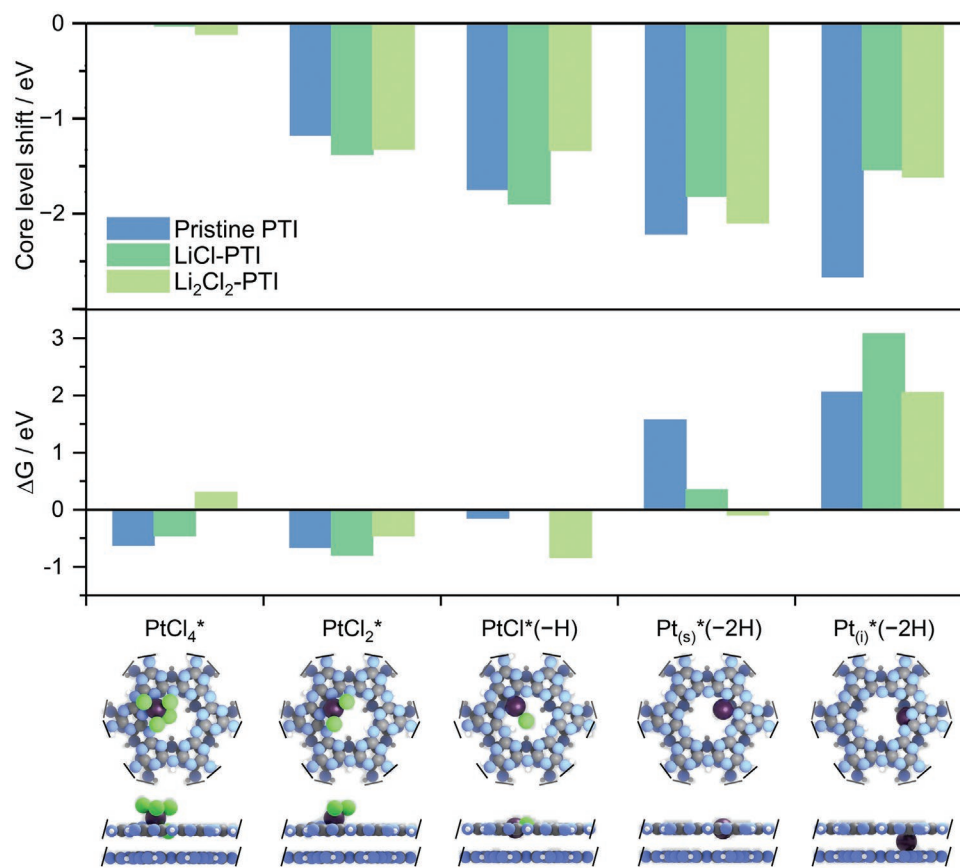


**Figure 4.** Energetics of platinum stabilization in the cavity of poly(triazine imide) for distinct species with or without the presence of additional lithium and chlorine ions. The reference states are provided in Table S5 (Supporting Information). Schemes of adsorbed species on the pristine poly(triazine imide) are illustrated below in top- and side-view. Atom coloring: C, grey; H, white; N, blue; Cl, green; and Pt, purple.

(−1.73 eV for  $\text{PtCl}^*(-\text{H})$  and −2.19 eV for  $\text{Pt}_{(\text{s})}^*(-2\text{H})$ ) compared to the physisorbed precursor ( $\text{PtCl}_4^*$ ). This observation is consistent with the increasing Pt–N coordination observed by XAS. Simulation of the corresponding EXAFS spectra can further confirm the evolution of the chemical environment of Pt (Figure S20, Supporting Information), where Pt–Cl patterns are lower for mono-Cl and Cl-free species, in line with the experimental characterization.

The adsorption profiles of  $\text{PtCl}_6^{2-}$  over a cavity containing one or two pairs of LiCl have a similar shape to the analog over the template-free scaffold (Table S5, Supporting Information), particularly for low-chlorinated species such as  $\text{PtCl}_2^*$  and  $\text{PtCl}^*(-\text{H})$ . Nonetheless, the interaction of the templating salt with the bare Pt ensemble ( $\text{Pt}_{(\text{s})}^*(-2\text{H})$ ) prominently stabilizes the single atom configuration by at least 1.2 eV. The presence of a second salt–ion pair further enhances the formation of  $\text{Pt}_{(\text{s})}^*(-2\text{H})$  by 0.4 eV, even surpassing the energetic cost for the interaction of two LiCl molecules (0.2 eV). The favorable interaction of LiCl with Pt leads to higher core level shifts for the bare Pt ensemble (−1.80 or −2.08 eV in the presence of one or two LiCl pairs, respectively), indicating the stronger binding of the single metal atom to the scaffold.

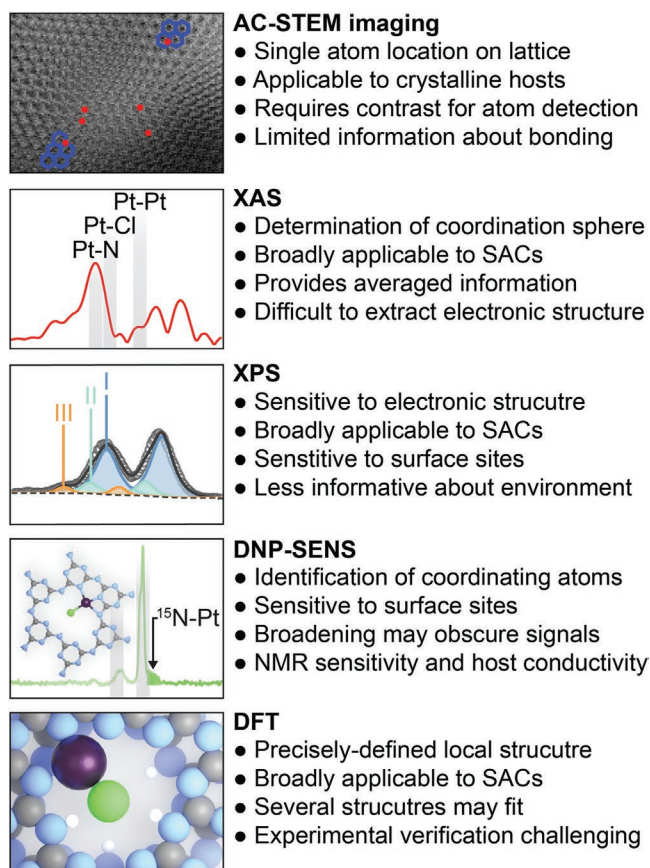
Independent of the exact speciation of the adsorbed Pt species on poly(triazine imide), Pt univocally sits at the corners of the triangular cavities bound to two  $N_b$  nitrogens (schemes in

Figure 4). The presence or absence of LiCl molecules in the cavity does not alter the preferred location of the platinum atoms (Figure S21, Supporting Information), indicating that they are also unlikely to have a major effect on the AC-STEM observations. Chlorine ligands lie in the center of the cavities in the carrier, potentially interacting with Li and Pt, thus forming ion rows that match the intensity patterns observed in simulated AC-STEM micrographs (Figure 1). Coordination sites of Pt in the interlayer region of PTI ( $\text{Pt}_{(\text{i})}^*(-2\text{H})$ ) are thermodynamically hindered by at least 0.5 eV.

## 2.5. Discussion

Through the advanced imaging and spectroscopy approaches applied in this work, we could experimentally elucidate the geometric and associated electronic structure of SACs based on carbon nitride with an unprecedented depth. Each technique provided complementary insights about distinct structural characteristics with different levels of granularity concerning the local environment (Figure 5). In particular, the simultaneous dose-limited BF-HAADF AC-STEM imaging enabled us to map the positions of platinum atoms onto the host lattice. Despite their prevalent use as hosts for single atoms, to the best of our knowledge, this is the first example where





**Figure 5.** Summary of the characterization approach applied to elucidate the geometric and electronic structure of SACs based on carbon nitride indicating the structural information derived, general applicability, and limitations of each technique.

crystallographic information from carbon nitrides was preserved during imaging of single-atom catalysts. This imaging strategy is potentially applicable to SACs based on other beam-sensitive and semicrystalline host materials (e.g., distinct forms of carbon nitride, crystalline organopolymers, and boron nitride). The main limitation is that although it is possible to confirm the approximate atom locations, it does not provide direct information about the bonding with the lattice.

XAS was the most powerful tool to study the local environment of metal centers. While this technique is also broadly applicable to SACs and can follow the removal of ligands from the metal precursor during the synthesis, evidencing coordination numbers in close agreement with the predicted trend, it is difficult to discriminate the specific interaction with the coordination sites. The impact of the geometric structure on the XANES spectra also complicates the interpretation of the electronic properties. In this regard, XPS gave the most direct information about the electronic structure of the metal species, and by following the changes at different stages of the synthesis we could correlate them with the oxidative and reductive processes occurring, but it is not straightforward to extract information about the local environment.

Comparatively, DNP-SENS of  $^{15}\text{N}$  nuclei, applied for the first time to study metal–host interactions in SACs, enabled the

most precise understanding of the interaction of the metal with the host. It confirmed the increased bonding of Pt atoms to nitrogen coordination sites upon removal of the ligands of the precursor and, when coupled with DFT simulations to assign chemical shifts, could identify the most likely bonding configuration of the metal centers. The applicability of DNP-SENS is limited by the sensitivity of individual nuclei as well as the conductivity of host materials. However, the demonstrated effectiveness of  $^{15}\text{N}$  analysis makes it broadly applicable to SACs based on carbon nitrides, and the study of other nuclei (e.g.,  $^{13}\text{C}$ ,  $^{17}\text{O}$ , and  $^{31}\text{P}$ ) could give insights into metal coordination in other hosts.<sup>[20]</sup>

DFT enables the exploration of precisely defined structural models of virtually any SAC and has provided an advanced understanding of the properties of metal atoms stabilized on carbon nitrides in distinct catalytic applications.<sup>[17]</sup> A positive outcome of this study is the good agreement obtained between experimentally evidenced and DFT simulated structures, providing the most robust benchmark to date for the structural assumptions underlying the models. Even when considering ideal crystalline structures, the simulations reveal the potential coexistence of multiple structures that are not easy to discriminate experimentally. The possible nonuniformity of single-atom structures was also clearly revealed by the AC-STEM and XPS analysis, emphasizing the need to account for distributions of active site structures. Nonetheless, even within the disordered regions of the host, terminal nitrogen defect site ( $N_c$  and  $N_d$ , Figure 1c) was not detected by DNP-enhanced  $^1\text{H}$ - $^{15}\text{N}$  CP/MAS NMR spectroscopy analysis, suggesting a high degree of condensation of the triazine units. Our findings also highlight the strong dependence of the structure on the synthesis conditions, emphasizing the importance of monitoring changes in the local environment during catalyst preparation.

### 3. Conclusions

In summary, we elucidated the local atomic environment of platinum atoms stabilized on a form of carbon nitride with extended crystalline domains. Detailed analysis by AC-STEM, XPS, and DNP-enhanced  $^{15}\text{N}$  NMR spectroscopy confirmed the uniformity of coordination sites, comprising mainly C-NH-C and pyridinic N sites, in this host material. Simultaneous dose-limited BF-HAADF imaging by AC-STEM revealed that fully stabilized Pt species prefer to locate in-plane within the triazine layers at the corners of the triangular motifs in the poly(triazine imide) lattice. Analysis of the coordination environment after different steps in the synthesis highlighted the dependence on the conditions applied. Complementing the insights gained into the removal of chlorine ligands and coordination to nitrogen by EXAFS, DNP-SENS showed that platinum atoms primarily bond to pyridinic N species, and the interaction is strongest after high-temperature activation to remove all ligands from the precursor. The imaging also highlighted metal coordinated to amorphous regions of the sample, emphasizing the potential diversity of local atomic environments present in SACs. The experimental results generally agreed well with computational data, which also identified a thermodynamic preference for the metal to coordinate in the corner of the cavities within the

triazine layers. DFT simulations also predicted the potential coexistence of multiple structures with different intercalated ions or degrees of chlorination. The multi-technique approach reported provides an advanced platform for analyzing metal coordination spheres in carbon nitrides, necessary to develop improved design principles for single-atom catalysts.

## 4. Experimental Section

**Material Synthesis:** All chemicals were obtained from Sigma–Aldrich unless otherwise specified. Poly(triazine imide) carriers were synthesized by adapting a previously reported procedure.<sup>[14]</sup> Standard (PTI) and highly crystalline (HC-PTI) forms were prepared by ball milling eutectic salt mixtures containing LiCl (4.52 g) and KCl (5.48 g) for PTI and LiCl (10 g) for HC-PTI together with melamine (1 g) for 10 min (Retsch Mixer Mill MM 500, 20 Hz). Afterward, the mixtures were transferred into a crucible and polymerization was started by heating at 823 K for 4 h (2.3 K min<sup>-1</sup> ramp) under a nitrogen flow (20 cm<sup>3</sup> min<sup>-1</sup>). The resulting materials were washed in hot water (353 K, 500 cm<sup>3</sup>) for 48 h to remove any excess salts. Finally, the poly(triazine imides) were collected by filtration, washed with distilled water (250 cm<sup>3</sup>) and ethanol (125 cm<sup>3</sup>), and dried in air at 338 K overnight. Platinum single atoms were introduced following a versatile two-step procedure developed to enable the controlled coordination of metal precursors to supports.<sup>[25]</sup> In a typical synthesis, the carrier material (PTI or HC-PTI, 0.5 g) was mixed with hexachloroplatinic acid (H<sub>2</sub>PtCl<sub>6</sub>, targeted Pt contents of 0.5 or 5 wt.%), dissolved in water (25 cm<sup>3</sup>). After sonication for 1 h, the solvent was evaporated by rotary evaporation and the resulting powder was subjected to a first thermal activation step ( $T_{A1} = 473\text{--}573$  K, 5 h, 5 K min<sup>-1</sup> ramp) in flowing nitrogen (20 cm<sup>3</sup> min<sup>-1</sup>). The samples were subsequently washed in hot dimethyl sulfoxide (375 cm<sup>3</sup>, 353 K) to remove loosely bound metal species, then filtered and washed with water (623 cm<sup>3</sup>). The resulting powder was dried and subjected to a second thermal activation step ( $T_{A2} = 573\text{--}773$  K, 5 h, 2 K min<sup>-1</sup> ramp) in flowing nitrogen (20 cm<sup>3</sup> min<sup>-1</sup>). For comparison, intermediate samples were also isolated after the metal impregnation (Pt<sub>IMP</sub>/PTI), the first thermal activation (Pt<sub>A1</sub>/PTI), and the washing steps (Pt<sub>WASH</sub>/PTI). Specific synthesis parameters and sample codes for all presented materials are summarized in Table S2 (Supporting Information).

**Basic Characterization:** Powder X-ray diffraction (XRD) was performed in a PANalytical X'Pert PRO-MPD diffractometer in Bragg–Brentano geometry using Ni-filtered Cu K $\alpha$  radiation ( $\lambda = 0.1541$  nm, data range = 5–40° 2 $\theta$ , step size = 0.05°, counting time = 2 s step<sup>-1</sup>). Argon sorption at 77 K was measured using a Micrometrics 3Flex instrument after evacuating the samples at 423 K for 7 h. The surface area was estimated using the Brunauer–Emmett–Teller (BET) method. Elemental analysis was undertaken using LECO TruSpec Micro (C, H, and N) and LECO 628 O Micro (O) instruments. Inductively coupled plasma-optical emission spectrometry (ICP-OES) was conducted using a Horiba Ultra 2 instrument equipped with photomultiplier tube detection. Catalyst powders were dissolved by heating the sample ( $\approx 10$  mg) in 3 cm<sup>3</sup> of acid solution to 533 K for 50 min in an MLS turboWave microwave (maximum power = 1200 W, loading pressure = 70 bar). The acid solution consisted of volumetric ratios 3:1 nitric acid (65 wt.%) and hydrogen peroxide (35 wt.%) for metal-free materials and 3:1:2 nitric acid, hydrogen peroxide, and hydrochloric acid (37 wt.%) in the case of platinum-containing samples. The obtained clear solutions were diluted to 25 cm<sup>3</sup> and filtered (pore size, 0.45  $\mu$ m) prior to analysis.

**Advanced Imaging:** Aberration-corrected scanning transmission electron microscopy (AC-STEM) imaging was performed using a Nion UltraSTEM100 equipped with a cold field emission gun (CFEG) and a Nion aberration corrector in the probe-forming lenses, operated at 60 kV with an incident convergence semi-angle of 32 mrad. AC-STEM images were recorded with a high-angle annular dark-field detector (HAADF, 90–185 mrad collection semi-angle) as well as with a bright-field detector (BF, <5 mrad collection semi-angle). The operation at 60 kV reduced

the energy transfer to displace atoms in the sample (reduced knock-on damage). In selecting STEM electron beam energies (operating voltage), there was generally a trade-off between reduced knock-on damage at lower accelerating voltages and increased radiolysis (ionization induced bond breaking) due to higher ionization cross-sections at lower accelerating voltages. Both of these damage mechanisms presented challenges for SAC imaging, as displacement of transition metal species would introduce ambiguity in catalytic sites and loss of structural order in the support precludes correlation between metal species and the host lattice. The beam current was estimated at 40 pA and a per-pixel dwell time of 38.7  $\mu$ s. To maintain comparable beam currents, the CFEG tip was flashed every 2 h. Images were acquired at 1024  $\times$  1024 pixels, with a pixel size of either 0.08 or 0.1 nm. Electron beam current, exposure time, and pixel size were selected to balance sufficient signal-to-noise for single metal atom visibility while minimizing beam-induced changes. The resolution was monitored regularly throughout the experiment on the graphene support film and aberration corrector parameters were adjusted to maintain a consistent probe size at the sample.

BF-STEM image filtering was carried out in Gatan Microscopy Suite software, using circular array masks on the Fourier transform. The masked Fourier transform was then inverted to produce a filtered image. HAADF-STEM image filtering was carried out in ImageJ software by first applying a median filter (15-pixel kernel) to produce an image without fine-scale intensity variations. This smoothed image was subtracted from the originally acquired image to produce an image highlighting the fine-scale variations only. A Gaussian blur (0.9 pixels) was applied to reduce high-frequency noise.

AC-STEM imaging at 300 kV was performed at a double Cs corrected microscope JEM-ARM300F (GrandARM, JEOL, electron gun: cold-field emitter;  $\Delta E = 0.35$  eV, equipped with an energy-dispersive X-ray spectroscopy detector) with a probe convergence semi-angle of 18 mrad. Annular dark-field STEM images were recorded with 33–106 mrad collection semi-angles. Annular bright-field STEM images were recorded with 12–24 mrad collection semi-angle. All TEM micrographs were measured at low-dose illumination conditions with current densities of  $\approx 0.3$  pA cm<sup>-3</sup> measured on the small viewing screen. For this TEM study, the specimens were prepared by drop deposition of nanoparticles dispersed in isopropanol onto a copper grid with a lacey carbon support film. Image simulation was performed using JEMS software.

**Spectroscopic Approaches:** X-ray photoelectron spectroscopy (XPS) was measured using a Physical Electronics Quatera SXM spectrometer using monochromatic Al K $\alpha$  radiation (1486.6 eV, electron beam operated at 15 kV and 49.3 W, spot size = 200  $\mu$ m, electron, and ion neutralizer operated simultaneously). Samples were mounted by pressing finely ground powders onto indium foil (Alfa Aesar, 99.99 %). The peak of adventitious carbon in PTI was referenced to 284.8 eV, yielding a peak position for CN<sub>3</sub> of 287.9 eV. This value was applied for the energy correction of all other samples. A constant pass energy of 55.0 eV was applied to yield a full width at half maximum of below 1 eV for Au 4f<sub>7/2</sub>. The elemental concentrations were quantified based on the measured photoelectron peak areas (C 1s, N 1s, O 1s, Li 1s, Cl 2p, and Pt 4f) using the theoretical photoionization cross-sections as the relative sensitivity factors.<sup>[27]</sup>

The <sup>15</sup>N dynamic nuclear polarization surface-enhanced nuclear magnetic resonance spectroscopy (DNP-SENS) experiments were performed on a Bruker 600 MHz (14.1 T) spectrometer by using a 3.2 mm HXY DNP probe in a double-mode (<sup>1</sup>H/<sup>15</sup>N) configuration. A gyrotron generated microwaves with a power of  $\approx 6$  W at 395 GHz to drive the DNP cross effect. All samples were prepared by wetness impregnation with 16  $\times 10^{-6}$  M TEKPol solution in TCE (1,1,2,2-tetrachloroethane). Typically, for 15 mg of the sample 0.03–0.05 cm<sup>3</sup> of radical solution was required to fully impregnate the sample; the mixture was directly packed into a 3.2 mm sapphire rotor with zirconia cap. The sapphire rotors were used for optimal microwave penetration. Rotors were inserted in the cryogenic probe within a short period of time ( $\approx 5$  min) and cooled to 100 K by a cryogenic heat exchanger system. In all the measurements, the magic-angle spinning (MAS) rate was set to 8 kHz. The spectra were recorded using <sup>1</sup>H-<sup>15</sup>N CP/MAS pulse sequence with the contact time of



2 ms. The DNP enhancement of solvent (TCE) obtained was found to be 24, which allowed for the successful characterization of the samples with the natural abundance of  $^{15}\text{N}$ . Chemical shifts obtained in the  $^{15}\text{N}$  NMR spectra were indirectly referenced by adjusting the  $^1\text{H}$  NMR signal of TCE to 6.9 ppm. Bruker Topspin 3.2 software package was used for data acquisition and processing.

X-ray absorption fine structure (XAFS) measurements at the Pt  $L_3$ -edge were carried out at the SuperXAS beamline at the Swiss Light Source (Villigen, Switzerland). The incident photon beam provided by a 2.9 T superbend magnet was selected by a Si(111) channel-cut Quick-EXAFS monochromator. The rejection of higher harmonics and focusing were achieved with rhodium-coated collimating and toroidal mirrors, respectively, at 2.9 and 2.5 mrad. The beamline was calibrated using Pt foil. The area of sample illuminated by the X-ray beam was 1.0 mm  $\times$  0.3 mm. Optimal amounts of samples were finely ground and filled inside a 0.5 cm wide cylindrical tube closed on the two sides with Kapton windows and measured in transmission geometry along the tube length at room temperature. The XAFS spectra across the Pt  $L_3$ -edge were acquired with a 1 Hz frequency (0.5 s per spectrum) and then averaged over 5 min. The energy was calibrated by measuring Pt foil simultaneously with each sample. The XAFS spectra were calibrated and averaged using ProQEXAFS software and analyzed using the Demeter software package. The background signal before the Pt  $L_3$ -edge was subtracted using a linear function (fitting range between  $-150$  and  $-30$  eV). The post-edge signal was normalized to the step of one after fitting it in the region between 150 and 1300 eV after the edge. The  $k^3$  weighted Fourier transformed signal was fitted and an amplitude reduction factor ( $S_0^2$ ) of 0.85 from EXAFS fit of the Pt metal foil was determined. All EXAFS spectra were fitted for the first coordination shell in the  $k$ -range of 3–12  $\text{\AA}^{-1}$  and  $R$ -range of 1–3  $\text{\AA}$ . Pt,  $\text{PtCl}_2$ , and  $\text{PtO}_2$  were used as references for fitting.

**Computational Details:** DFT on models of the platinum-doped poly(triazine imide) structures was employed as implemented in the Vienna ab initio Simulation Package (VASP 5.4.4).<sup>[28]</sup> The generalized gradient approximation of the Perdew-Burke-Ernzerhof functional (GGA-PBE)<sup>[29]</sup> was used to obtain the exchange-correlation energies with dispersion contributions introduced via Grimme's DFT-D3 approach.<sup>[30]</sup> Projector augmented wave (PAW)<sup>[31]</sup> and plane waves with a cut-off energy of 450 eV, with spin polarization allowed when needed, were chosen to represent the inner electrons and the valence monoelectronic states, respectively. For simulation of the support, a four-layer slab of poly(triazine imide) with 9N per cavity separated by 1  $\text{\AA}$  of vacuum was used and sampled through a gamma-centered grid of  $3 \times 3 \times 1$  k-points. Different initial contents of LiCl in PTI were also considered. Pt-doped poly(triazine imide) structures were modelled by placing  $\text{PtCl}_x$  ( $x = 0-6$ ) units in the center of the cavity. The three top layers and the adsorbates were allowed to relax while the bottom one was fixed to the bulk lattice. The arising dipole was corrected in all slab models.<sup>[32]</sup> Gas-phase molecules were optimized in a box of  $14.0 \times 14.5 \times 15.0 \text{\AA}^3$ . For all investigated systems, structures were relaxed using convergence criteria of  $10^{-4}$  and  $10^{-5}$  eV for the ionic and electronic steps, respectively. To assess the stability of Pt structures in the PTI, Gibbs free formation energies were estimated using the water-solvated metal precursor ( $\text{PtCl}_6^{2-}$ ),  $\text{H}_2$ , HCl, LiCl, and the support as reference states. The solvation energy for the metal precursor was calculated using the SMD model<sup>[33]</sup> as implemented in Gaussian09,<sup>[34]</sup> with a resultant value coinciding with previous reports.<sup>[35]</sup> The 6-31 g basis set<sup>[36]</sup> was used for all atoms and a General Gradient Approximation (GGA) based density functional (PBE) was included in both calculations (gas-phase, water-solvent).

Entropic contributions from molecules were considered. Only one possible structure for each system was considered. The energy differences when removing ligands were large enough to ensure that the considered resting states were representative. Furthermore, the scaffold limited the fluxionality of the structures. All the structures presented in this work had been uploaded to the ioChem-BD database.<sup>[37]</sup>

**DFT Calculation of NMR Parameters:** The clusters were cut from the periodic structure using Material Studio 8.0 software package. In

the top layer of the PTI or Pt-PTI surface, one triangular window was cut as shown in Figure 1c and Figure S17 (Supporting Information). Consequently, H-atoms in the cluster edges were allowed to fully relax, while N, C, Pt, Li, Cl, and H inside the triangular pockets were fixed. For the output structures, DFT simulations of NMR spectroscopic parameters were conducted. All geometry optimizations of clusters were performed with the Gaussian09<sup>[38]</sup> package with the PBE0<sup>[39]</sup> hybrid functional. H, C, and N atoms were represented by a triple- $\zeta$  pcseg-2 basis set.<sup>[40]</sup> NMR simulations were performed within the GIAO framework using ADF 2016<sup>[41]</sup> with the PBE0 functional and Slater-type basis sets of triple- $\zeta$  quality (TZ2P). Pyridine, calculated at the same level of theory and referenced to 317 ppm,<sup>[42]</sup> was used as the reference for chemical shifts, was calculated at the same level of theory.

## Supporting Information

Supporting Information is available from the Wiley Online Library or from the author.

## Acknowledgements

This publication was created as part of NCCR Catalysis (180544), a National Centre of Competence in Research funded by the Swiss National Science Foundation. A.Y. gratefully acknowledges the ETH Career Seed Grant for funding. A.Y. and C.C. thank ETH+ Project SynMatLab for financial support and Dr. Miroslav Peterek and Dr. Marc Georg Willinger for helpful discussions. The SuperXAS beamline at PSI, and SuperSTEM, the U.K. National Facility for Advanced Electron Microscopy funded by the Engineering and Physical Sciences Research Council, for access to their facilities. BSC-RES for providing computational resources.

Open access funding provided by Eidgenössische Technische Hochschule Zurich.

## Conflict of Interest

The authors declare no conflict of interest.

## Data Availability Statement

All data supporting this article will be made publicly available upon its publication. Experimental data are shared through Zenodo (doi:10.5281/zenodo.6359849), and simulations are shared through the ioChem database (<https://iochem-bd.iciq.es/browse/review-collection/100/38849/ee5f8671e8c0d71720574360>).

## Keywords

carbon nitrides, characterization, metal coordination sites, metal speciation, single-atom catalysis

Received: April 2, 2022

Revised: May 5, 2022

Published online:

- [1] a) A. Wang, J. Li, T. Zhang, *Nat. Rev. Chem.* **2018**, *2*, 65; b) S. K. Kaiser, Z. Chen, D. Faust Akl, S. Mitchell, J. Pérez-Ramírez, *Chem. Rev.* **2020**, *120*, 11703; c) R. T. Hannagan, G. Giannakakis, M. Flytzani-Stephanopoulos, E. C. H. Sykes, *Chem. Rev.* **2020**, *120*, 12044; d) M. D. Korzyński, C. Copéret, *Trends Chem.* **2021**, *3*, 850.

- [2] a) W.-H. Lai, Z. Miao, Y.-X. Wang, J.-Z. Wang, S.-L. Chou, *Adv. Energy Mater.* **2019**, *9*, 1900722; b) T. Sun, S. Mitchell, J. Li, P. Lyu, X. Wu, J. Pérez-Ramírez, J. Lu, *Adv. Mater.* **2021**, *33*, 2003075; c) X. Li, L. Liu, X. Ren, J. Gao, Y. Huang, B. Liu, *Sci. Adv.* **2020**, *6*, eabb6833.
- [3] a) P. Christopher, *ACS Energy Lett.* **2019**, *4*, 2249; b) B. Peng, H. Liu, Z. Liu, X. Duan, Y. Huang, *J. Phys. Chem. Lett.* **2021**, *12*, 2837.
- [4] J. Resasco, L. DeRita, S. Dai, J. P. Chada, M. Xu, X. Yan, J. Finzel, S. Hanukovich, A. S. Hoffman, G. W. Graham, S. R. Bare, *J. Am. Chem. Soc.* **2020**, *142*, 169.
- [5] a) S. Mitchell, J. Pérez-Ramírez, *Nat. Rev. Mater.* **2021**, *6*, 969; b) X. Li, X. Yang, J. Zhang, Y. Huang, B. Liu, *ACS Catal.* **2019**, *9*, 2521; c) G. Parkinson, *Chin. J. Catal.* **2017**, *38*, 1454.
- [6] P. Tieu, X. Yan, M. Xu, P. Christopher, X. Pan, *Small* **2021**, *17*, 2006482.
- [7] a) Y. Cheng, S. Zhao, H. Li, S. He, J.-P. Veder, B. Johannessen, J. Xiao, S. Lu, J. Pan, M. F. Chisholm, S.-Z. Yang, C. Liu, J. G. Chen, S. P. Jiang, *Appl. Catal. B* **2019**, *243*, 294; b) Q. M. Ramasse, C. R. Seabourne, D.-M. Kepaptsoglou, R. Zan, U. Bangert, A. J. Scott, *Nano Lett.* **2013**, *13*, 4989; c) D. A. Bulushev, M. Zacharska, A. S. Lisitsyn, O. Y. Podyacheva, F. S. Hage, Q. M. Ramasse, U. Bangert, L. G. Bulusheva, *ACS Catal.* **2016**, *6*, 3442.
- [8] a) T.-Y. Chang, Y. Tanaka, R. Ishikawa, K. Toyoura, K. Matsunaga, Y. Ikuhara, N. Shibata, *Nano Lett.* **2014**, *14*, 134; b) Y. Zhao, K. R. Yang, Z. Wang, X. Yan, S. Cao, Y. Ye, Q. Dong, X. Zhang, J. E. Thorne, L. Jin, K. L. Materna, *Proc. Nat. Acad. Sci.* **2018**, *115*, 2902; c) D. Kunwar, S. Zhou, A. DeLaRiva, E. J. Peterson, H. Xiong, X. I. Pereira-Hernández, S. C. Purdy, R. ter Veen, H. H. Brongersma, J. T. Miller, H. Hashiguchi, *ACS Catal.* **2019**, *9*, 3978.
- [9] G. Sun, Z.-J. Zhao, R. Mu, S. Zha, L. Li, S. Chen, K. Zang, J. Luo, Z. Li, S. C. Purdy, A. J. Kropf, J. T. Miller, L. Zeng, J. Gong, *Nat. Commun.* **2018**, *9*, 4454.
- [10] a) S. K. Kaiser, R. Lin, S. Mitchell, E. Fako, F. Krumeich, R. Hauert, O. V. Safonova, V. A. Kondratenko, E. V. Kondratenko, S. M. Collins, P. A. Midgley, N. López, J. Pérez-Ramírez, *Chem. Sci.* **2019**, *10*, 359; b) Q. Chen, C. Dwyer, G. Sheng, C. Zhu, X. Li, C. Zheng, Y. Zhu, *Adv. Mater.* **2020**, *32*, 1907619.
- [11] Y. Li, A. I. Frenkel, *Acc. Chem. Res.* **2021**, *54*, 2660.
- [12] L. Li, X. Chang, X. Lin, Z. J. Zhao, J. Gong, *Chem. Soc. Rev.* **2020**, *49*, 8156.
- [13] a) X. Li, P. Cui, W. Zhong, J. Li, X. Wang, Z. Wang, J. Jiang, *Chem. Commun.* **2016**, *52*, 13233; b) G. Gao, Y. Jiao, E. R. Waclawik, A. Du, *J. Am. Chem. Soc.* **2016**, *138*, 6292; c) J. Wang, P. Kumar, H. Zhao, M. G. Kibria, J. Hu, *Green Chem.* **2021**, *23*, 7435.
- [14] Z. Chen, E. Vorobyeva, S. Mitchell, E. Fako, N. López, S. M. Collins, R. K. Leary, P. A. Midgley, R. Hauert, J. Pérez-Ramírez, *Natl. Sci. Rev.* **2018**, *5*, 642.
- [15] a) A. Thomas, A. Fischer, F. Goettmann, M. Antonietti, J. O. Müller, R. Schlögl, J. M. Carlsson, *J. Mater. Chem.* **2008**, *18*, 4893; b) T. S. Miller, A. B. Jorge, T. M. Suter, A. Sella, F. Corà, P. F. McMillan, *Phys. Chem. Chem. Phys.* **2017**, *19*, 15613; c) M. A. da Silva, I. F. Silva, Q. Xue, B. T. Lo, N. V. Tarakina, B. N. Nunes, P. Adler, S. K. Sahoo, D. W. Bahnemann, N. López-Salas, A. Savateev, *Appl. Catal. B: Environ.* **2022**, *304*, 120965.
- [16] a) L. Lin, Z. Lin, J. Zhang, X. Cai, W. Lin, Z. Yu, X. Wang, *Nat. Catal.* **2020**, *3*, 649; b) W. Wang, J. Cui, Z. Sun, L. Xie, X. Mu, L. Huang, J. He, *Adv. Mater.* **2021**, *33*, 2106359; c) K. Schwinghammer, B. Tuffy, M. B. Mesch, E. Wirnhier, C. Martineau, F. Taulelle, W. Schnick, J. Senker, B. V. Lotsch, *Angew. Chem., Int. Ed.* **2013**, *52*, 2435.
- [17] a) Z. Chen, S. Mitchell, E. Vorobyeva, R. K. Leary, R. Hauert, T. Furnival, Q. M. Ramasse, J. M. Thomas, P. A. Midgley, D. Dontsova, M. Antonietti, S. Pogodin, N. López, J. Pérez-Ramírez, *Adv. Funct. Mater.* **2017**, *27*, 1605785; b) Z. Chen, E. Vorobyeva, S. Mitchell, E. Fako, M. A. Ortuño, N. López, S. M. Collins, P. A. Midgley, S. Richard, G. Vilé, J. Pérez-Ramírez, *Nat. Nanotechnol.* **2018**, *13*, 702.
- [18] a) E. Wirnhier, M. Döblinger, D. Gunzelmann, J. Senker, B. V. Lotsch, W. Schnick, *Chem. - Eur. J.* **2013**, *17*, 3213; b) Z. Chen, A. Savateev, S. Pronkin, V. Papaefthimiou, C. Wolff, M. G. Willinger, E. Willinger, D. Neher, M. Antonietti, D. Dontsova, *Adv. Mater.* **2017**, *29*, 1700555.
- [19] M. B. Mesch, K. Bärwinkel, Y. Krysiak, C. Martineau, F. Taulelle, R. B. Neder, U. Kolb, J. Senker, *Chem. - Eur. J.* **2016**, *22*, 16878.
- [20] D. Burmeister, H. A. Tran, J. Müller, M. Guerrini, C. Cocchi, J. Plaickner, Z. Kochovski, E. J. List-Kratochvil, M. J. Bojds, *Angew. Chem., Int. Ed.* **2022**, *61*, e202111749.
- [21] A. Rossini, *J. Phys. Chem. Lett.* **2018**, *9*, 5150.
- [22] a) A. J. Rossini, A. Zagdoun, F. Hegner, M. Schwarzwald, D. Gajan, C. Copéret, A. Lesage, L. Emsley, *J. Am. Chem. Soc.* **2012**, *134*, 16899; b) T. Kobayashi, F. A. Perras, I. I. Slowing, A. D. Sadow, M. Pruski, *ACS Catal.* **2015**, *5*, 7055; c) A. J. Rossini, A. Zagdoun, M. Lelli, A. Lesage, C. Copéret, L. Emsley, *Acc. Chem. Res.* **2013**, *46*, 1942.
- [23] a) R. S. Pantelic, J. C. Meyer, U. Kaiser, H. Stahlberg, *Solid State Commun.* **2012**, *152*, 1375; b) R. Zan, Q. M. Ramasse, R. Jalil, T. Georgiou, U. Bangert, K. S. Novoselov, *ACS Nano* **2013**, *7*, 10167.
- [24] S. Mitchell, F. Parés, D. Faust Akl, S. Collins, D. Kepaptsoglou, Q. Ramasse, D. Garcia-Gasulla, J. Pérez-Ramírez, N. López, *J. Am. Chem. Soc.* **2022**, *144*, 8018.
- [25] X. Hai, S. Xi, S. Mitchell, K. Harrath, H. Xu, D. Faust Akl, D. Kong, J. Li, Z. Li, T. Sun, H. Yang, Y. Cui, C. Su, X. Zhao, J. Li, J. Pérez-Ramírez, J. Lu, *Nat. Nanotechnol.* **2022**, *17*, 174.
- [26] Z. Zhang, Y. Chen, L. Zhou, C. Chen, Z. Han, B. Zhang, Q. Wu, L. Yang, L. Du, Y. Bu, P. Wang, X. Wang, H. Yang, Z. Hu, *Nat. Commun.* **2019**, *10*, 1657.
- [27] Z. Jin, Z. Chen, Q. Li, C. Xi, X. Zheng, *J. Photochem. Photobiol., A* **1994**, *81*, 177.
- [28] a) G. Kresse, J. Furthmüller, *Phys. Rev. B* **1996**, *54*, 11169; b) G. Kresse, J. Furthmüller, *Comput. Mater. Sci.* **1996**, *6*, 15.
- [29] J. P. Perdew, K. Burke, M. Ernzerhof, *Phys. Rev. Lett.* **1996**, *77*, 3865.
- [30] S. Grimme, J. Antony, S. Ehrlich, H. Krieg, *J. Chem. Phys.* **2010**, *132*, 154104.
- [31] a) P. E. Blöchl, *Phys. Rev. B* **1994**, *50*, 17953; b) G. Kresse, D. Joubert, *Phys. Rev. B* **1999**, *59*, 1758.
- [32] G. Makov, M. C. Payne, *Phys. Rev. B* **1995**, *51*, 4014.
- [33] A. V. Marenich, C. J. Cramer, D. G. Truhlar, *J. Phys. Chem. B* **2009**, *113*, 6378X.
- [34] M. J. Frisch, G. W. Trucks, H. B. Schlegel, G. E. Scuseria, M. A. Robb, J. R. Cheeseman, G. Scalmani, V. Barone, B. Mennucci, G. A. Petersson, H. Nakatsuji, M. Caricato, X. Li, H. P. Hratchian, A. F. Izmaylov, J. Bloino, G. Zheng, J. L. Sonnenberg, M. Hada, M. Ehara, K. Toyota, R. Fukuda, J. Hasegawa, M. Ishida, T. Nakajima, Y. Honda, O. Kitao, H. Nakai, T. Vreven, J. A. Montgomery Jr., et al., *Revision A-02*, Gaussian Inc., Wallingford, CT **2016**.
- [35] A. Uysal, W. Rock, B. Qiao, W. Bu, B. Lin, *J. Phys. Chem. C* **2017**, *121*, 25377.
- [36] a) R. Ditchfield, W. Hehre, J. A. Pople, *J. Chem. Phys.* **1971**, *54*, 724; b) P. C. Hariharan, J. A. Pople, *Theor. Chim. Acta* **1973**, *28*, 213; c) W. Hehre, R. Ditchfield, J. A. Pople, *J. Chem. Phys.* **1972**, *56*, 2257.
- [37] a) M. Álvarez-Moreno, C. de Graaf, N. López, F. Maseras, J. M. Poblet, C. Bo, *J. Chem. Inf. Model.* **2015**, *55*, 95; b) A. Ruiz-Ferrando, Pt/PTI Dataset, ioChem-BD database, **2022**, <https://iochem-bd.iciq.es/browse/review-collection/100/38849/ee5f8671e8c0d71720574360>.
- [38] M. J. Frisch, G. W. Trucks, H. B. Schlegel, G. E. Scuseria, M. A. Robb, J. R. Cheeseman, G. Scalmani, V. Barone, B. Mennucci, G. A. Petersson, H. Nakatsuji, X. Li, M. Caricato, A. Marenich, J. Bloino, B. G. Janesko, R. Gomperts, B. Mennucci, H. P. Hratchian, J. V. Ortiz, A. F. Izmaylov, J. L. Sonnenberg, D. Williams-Young, F. Ding, F. Lipparini, F. Egidi, J. Goings, B. Peng, A. Petrone,

- T. Henderson, et al., *Gaussian 09, revision D.01*, Gaussian, Inc., Wallingford, CT **2009**.
- [39] C. Adamo, V. Barone, *J. Chem. Phys.* **1999**, *110*, 6158.
- [40] F. Weigend, R. Ahlrichs, *Phys. Chem. Chem. Phys.* **2005**, *7*, 3297.
- [41] G. T. Te Velde, F. M. Bickelhaupt, E. J. Baerends, C. Fonseca Guerra, S. J. van Gisbergen, J. G. Snijders, T. Ziegler, *J. Comput. Chem.* **2001**, *22*, 931.
- [42] W. R. Gunther, V. K. Michaelis, R. G. Griffin, Y. Roman-Leshkov, *J. Phys. Chem. C* **2016**, *120*, 28533.